3-28-2012

M + Ng Potential Energy Curves Including Spin-orbit Coupling for M = K, Rb, Cs and Ng = He, Ne, Ar

Larry Aaron Blank
Air Force Institute of Technology

David E. Weeks
Air Force Institute of Technology

Gary S. Kedziora
Dynamic Research Corporation

M + Ng potential energy curves including spin-orbit coupling for M = K, Rb, Cs and Ng = He, Ne, Ar ⊘

L Blank; David E. Weeks; Gary S. Kedziora

Check for updates

View Online   Export Citation   CrossMark

M + Ng potential energy curves including spin-orbit coupling for M = K, Rb, Cs and Ng = He, Ne, Ar

L Blank,[1] David E. Weeks,[1,a)] and Gary S. Kedziora[2]

[1]*Department of Engineering Physics, Air Force Institute of Technology, 2950 Hobson Way, WPAFB, Ohio 45433-7765, USA*
[2]*Dynamic Research Corporation, 2435 5th St., WPAFB, Ohio 45433-7765, USA*

The $X^2\Sigma_{1/2}^+$, $A^2\Pi_{1/2}$, $A^2\Pi_{3/2}$, and $B^2\Sigma_{1/2}^+$ potential energy curves and associated dipole matrix elements are computed for M + Ng at the spin-orbit multi-reference configuration interaction level, where M = K, Rb, Cs and Ng = He, Ne, Ar. Dissociation energies and equilibrium positions for all minima are identified and corresponding vibrational energy levels are computed. Difference potentials are used together with the quasistatic approximation to estimate the position of satellite peaks of collisionally broadened D2 lines. The comparison of potential energy curves for different alkali atom and noble gas atom combinations is facilitated by using the same level of theory for all nine M + Ng pairs.[http://dx.doi.org/10.1063/1.3696377]

INTRODUCTION

Collisionally induced spectral broadening plays an important role in the operation of optically pumped alkali laser (OPAL) systems by providing a mechanism with which the alkali D2 line can be broadened to more closely match the optical pump bandwidth.[1–5] This has generated interest in the collisionally induced spectral broadening of the D1 and D2 lines of alkali atoms as they interact with a variety of collisional partners.[6–10] Another class of lasing systems similar to the OPAL systems is the excimer pumped alkali vapor laser (XPAL).[9–15] These systems have been successfully demonstrated by Readle *et al.*[9] for a gas of Cs + Ar together with a small amount of ethane used to enhance the $^2P_{3/2} \rightarrow {}^2P_{1/2}$ transition rate. Instead of pumping the D2 line of the alkali atom, XPAL systems pump a collisionally induced satellite that is blue shifted from the D2 line. This satellite is associated with features of the potential energy curves (PECs) that govern the collisional dynamics of the cesium and argon atoms. Collisionally induced spectral broadening of the D1 and D2 alkali lines is also of interest to the astrophysical community as a possible diagnostic of brown dwarf atmospheres, which exhibit strong alkali absorption features that are spectrally broadened by collisions with helium and molecular hydrogen.[16–24]

Several theoretical models for collisional broadening exist and are reviewed by Szudy and Baylis[25] and Allard and Kielkopf.[26] To become predictive these models require knowledge of the interaction potentials between collision partners. As a first step in developing a theoretical understanding of the collisional line broadening processes that occur in OPAL systems, we compute the $X^2\Sigma_{1/2}^+$, $A^2\Pi_{1/2}$, $A^2\Pi_{3/2}$, and $B^2\Sigma_{1/2}^+$ PECs and corresponding dipole transition moments for M + Ng combinations, where M = K, Rb, Cs and Ng = He, Ne, Ar. The same level of theory is used to compute PECs for all nine M + Ng pairs facilitating the identification

of trends in well depth and equilibrium position. Previous calculations of the PECs for various M + Ng pairs have been carried out using a number of different methods. Early efforts by Pascale,[27] and more recently by Rhouma *et al.*,[28] employed pseudopotential techniques. Multi-reference configuration interaction calculations were carried out by Hirano *et al.*,[29] density functional theory (DFT) methods were employed by Zbiri and Daul,[30] a coupled-cluster approach was used by Merritt *et al.*,[31] and Goll *et al.*[32] performed a hybrid calculation using DFT and coupled-cluster methods.

The remainder of this paper is organized as follows. First, the method of calculation for the PECs and transition dipole moments is presented. This is followed by a quantitative discussion of the general features of the PECs. Finally, vibrational energy levels and blue shifted satellite positions are computed and compared with other calculations and experimental observations.

COMPUTATIONAL APPROACH

The $X^2\Sigma_{1/2}^+$, $A^2\Pi_{1/2}$, $A^2\Pi_{3/2}$, and $B^2\Sigma_{1/2}^+$ PECs and dipole transition moments of M + Ng are computed at the spin-orbit multi-reference singles and doubles configuration interaction (SOCI) level for M = K, Rb, Cs and Ng = He, Ne, Ar using the COLUMBUS suite of programs.[33–37] The small core Stuttgart relativistic pseudopotentials (PPs) and corresponding basis sets[38] are used for the alkali atoms in these calculations. These PPs consist of all but nine valance electrons for each alkali atom. For an ns^1 alkali atom, the nine valance electrons are the $(n-1)s^2$, $(n-1)p^6$, and ns^1 electrons. The Def2-TZVPP all electron segmented contracted GAUSSIAN basis sets[39] are used for the noble gas atoms.

The SOCI calculation employs state-averaged multi-configuration self-consistent field reference orbitals.[40] In terms of the dissociated atom limit, the $ns^1\,{}^2S$ ground and all three $np^1\,{}^2P$ excited states of the alkali atom are included in the state averaging procedure with equal weights. The

a)Electronic mail: david.weeks@afit.edu.

TABLE I. Various active space configurations labeled by the rubidium atomic orbitals for Rb + He at $R = 100$ Å. The first two configurations include a Davidson-Silver correction, and the largest configuration includes a renormalized Davidson correction (Ref. [42]). Energies are in cm^{-1}. The empirical NIST values for the $^2P_{1/2}$ and $^2P_{3/2}$ atomic excitation energies of Rb are 12 579 and 12 815 cm^{-1}, respectively (Ref. [41]). The Rb spin-orbit splitting, $\Delta = 236 \, cm^{-1}$.

Configuration	$^2P_{1/2}$	$^2P_{3/2}$	Δ
$5s5p$	12 555	12 754	199
$5s5p6s6p4d$	12 555	12 764	209
$5s5p6s6p4d7s7p5d$	12 591	12 804	213

complete active space consists of one electron in the ns and three np orbitals, and the resulting four configuration state functions (CSFs) comprise the reference space for the SOCI calculation. For these calculations all single and double excitations of the nine alkali electrons and the 2, 10, and 18 noble gas electrons, for He, Ne, and Ar, respectively, are used to generate the spin adapted CSFs that comprise the SOCI n electron basis. The maximum multiplicity of any of the CSFs is six, and the number of CSFs included in the SOCI calculations range from $\approx 10^6$ for K + He to $\approx 10^8$ for Cs + Ar. While significant computational savings occur when the core orbitals of Ne and Ar are frozen, slightly lower variational energies are obtained for our calculations by leaving all noble gas electrons active.

Several other active spaces were considered for various M + Ng combinations to explore possible improvements to the SOCI calculation. Each additional active space considered includes only the ns alkali electron and is extended beyond the $nsnp$ active space by including additional alkali atom orbitals. For Rb + He the additional active spaces are $5s5p6s6p4d$ and $5s5p6s6p4d7s7p5d$, and the corresponding SOCI results in the asymptotic limit of large R are summarized in Table I. In this limit, the SOCI energies approach the experimental D1 and D2 values[41] as the size of the active space increases. For smaller values of R the PECs computed using different active space configurations differ by nearly the same overall energy offset as observed in the asymptotic limit. As a result, all calculations are performed using an $nsnp$ orbital active space and offset in the asymptotic limit of $R = 100$ Å to the NIST D1 and D2 energies.[41] Specifically the $X^2\Sigma_{1/2}^+$ PECs are offset to zero, the $A^2\Pi_{1/2}$ PECs are offset to the $^2P_{1/2}$ energy, and the $A^2\Pi_{3/2}$ and $B^2\Sigma_{1/2}^+$ PECs are offset to the $^2P_{3/2}$ energy.

Upon completion of the SOCI calculation an *a posteriori* Davidson-Silver correction is performed to ameliorate size consistency error.[42] For Rb + Ne the Davidson-Silver correction introduces an overall offset in absolute energy of 9687 cm^{-1} for the $X^2\Sigma_{1/2}^+$ ground state and 9216 cm^{-1} for the $A^2\Pi_{1/2}$ and $A^2\Pi_{3/2}$ excited states. When the pre- and post-Davidson corrected surfaces are placed on the same energy scale, the ground state curve at equilibrium is deeper by 5.3 cm^{-1}, and the excited $A^2\Pi_{1/2}$ and $A^2\Pi_{3/2}$ curves at equilibrium are deeper by 28 and 33 cm^{-1}, respectively.

For these calculations we did not correct for basis set superposition error (BSSE). As a result we expect our calculations to somewhat over estimate well depths. The counter-
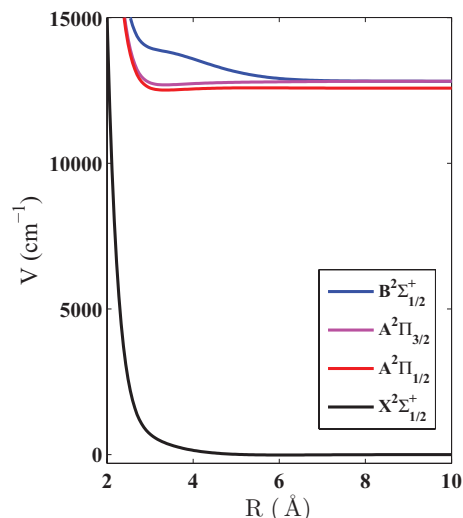

FIG. 1. The $X^2\Sigma_{1/2}^+$, $A^2\Pi_{1/2}$, $A^2\Pi_{3/2}$, and $B^2\Sigma_{1/2}^+$ curves of Rb + Ne. The asymptotic limit of the $X^2\Sigma_{1/2}^+$ curve is at 0 cm^{-1}. The excited curves are offset in the asymptotic limit to the NIST D1 (for $A^2\Pi_{1/2}$) and D2 (for $A^2\Pi_{3/2}$ and $B^2\Sigma_{1/2}^+$) values of Rb.[41]

poise (CP)[43] correction is often used to address BSSE. However, the CP technique tends to over correct for BSSE and yield an under estimate of the well depth.[44] It would appear that the best way to control for BSSE is to explore a hierarchy of basis sets to calculate energies with and without the CP correction.[45] For a suitably chosen hierarchy, the CP corrected and uncorrected energies will converge. In this case an extrapolation to the complete basis set limit is reasonable and will also eliminate basis set incompleteness error (BSIE). For many systems BSIE is significantly larger than BSSE[46] and is likely to be the largest source of error in our calculations. Both BSSE and BSIE occur in the ground and excited curves, and the degree to which they are present can be estimated by comparison with experiment and other theoretical calculations.

RESULTS AND DISCUSSION

The $X^2\Sigma_{1/2}^+$, $A^2\Pi_{1/2}$, $A^2\Pi_{3/2}$, and $B^2\Sigma_{1/2}^+$ PECs for Rb + Ne are shown in Figure 1. In the separated atom limit the $X^2\Sigma_{1/2}^+$ curve corresponds to the Rb $^2S_{1/2}$ ground state energy level, the $A^2\Pi_{1/2}$ curve corresponds to the Rb $^2P_{1/2}$ energy level, and the $A^2\Pi_{3/2}$ and $B^2\Sigma_{1/2}^+$ curves correspond to the Rb $^2P_{3/2}$ energy level. The $X^2\Sigma_{1/2}^+$ curve is mostly repulsive, with a shallow 14.4 cm^{-1} well in the region of $R \approx 6$ Å. The $B^2\Sigma_{1/2}^+$ curve also exhibits a shallow 0.7 cm^{-1} well further out toward the asymptotic limit in the range of $R \approx 9$ Å, as well as a shoulder on the repulsive wall at smaller values of R.

An expanded view of the excited state curves of Rb + Ne is shown in Figure 2 to exemplify details common to all M + Ng pairs. Moving in the direction of decreasing R from the asymptotic limit, the $A^2\Pi_{3/2}$ and the $B^2\Sigma_{1/2}^+$ curves diverge at approximately $R \approx 8.5$ Å. The $A^2\Pi_{3/2}$ curve decreases in energy below the asymptotic $^2P_{3/2}$ value and roughly follows the $A^2\Pi_{1/2}$ curve. These two $A^2\Pi$ curves exhibit relatively large
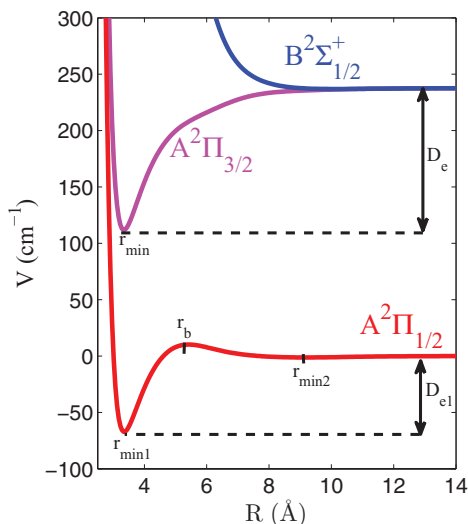
FIG. 2. The $A^2\Pi_{1/2}$, $A^2\Pi_{3/2}$, and $B^2\Sigma^+_{1/2}$ curves of Rb + Ne. The asymptotic limit of the $A^2\Pi_{1/2}$ curve is offset to $0\,\mathrm{cm}^{-1}$, and the asymptotic limit of the $A^2\Pi_{3/2}$ and $B^2\Sigma^+_{1/2}$ curves are offset to the NIST Rb spin-orbit splitting energy (Ref. 41). The $A^2\Pi_{3/2}$ curves for all M + Ng combinations have a single well at r_{min}, while most $A^2\Pi_{1/2}$ have two minima, one at r_{min1}, and the other at r_{min2}, separated by a barrier at r_b. The $B^2\Sigma^+_{1/2}$ curve also exhibits a shallow well not visible on the scale of this plot.

TABLE II. Equilibrium and barrier positions (Å), as defined in Figure 2, for all M + Ng curves. The pseudopotential calculations by Pascale (Ref. 27) and the DFT calculations by Zbiri and Daul (Ref. 30) report energies for the $A^2\Pi$ curve and are listed under both the $A^2\Pi_{1/2}$ and $A^2\Pi_{3/2}$ columns for ease of comparison.

M + Ng	$X^2\Sigma^+_{1/2}$ r_{min}	$A^2\Pi_{1/2}$ r_{min1}	r_b	r_{min2}	$A^2\Pi_{3/2}$ r_{min}	$B^2\Sigma^+_{1/2}$ r_{min}
KHe	6.35	2.86	6.72	9.42	2.86	10.27
Theo. (Ref. 30)	...	2.8	...	...	2.8	...
Theo. (Ref. 27)	...	2.8	...	...	2.8	...
KNe	5.66	3.12	7.20	8.15	3.12	9.42
Theo. (Ref. 32)	5.97	...	...	...	...	...
KAr	5.40	3.39	...	...	3.39	8.36
Exp. (Ref. 47)	5.3	...	...	...	...	...
Exp. (Ref. 48)	5.404(5)	3.37(3)	...	...	3.34(3)	7.10
Theo. (Ref. 28)	5.13	3.41	...	...	3.41	...
Theo. (Ref. 32)	5.322	...	...	...	...	...
RbHe	6.61	3.12	5.50	9.10	3.12	10.48
Theo. (Ref. 29)	...	3.21	5.3	...	3.21	...
Theo. (Ref. 30)	...	3.22	...	...	3.22	...
Theo. (Ref. 27)	...	3.3	...	...	3.3	...
RbNe	6.09	3.33	5.40	9.21	3.33	10.16
Theo. (Ref. 32)	6.19	...	...	...	...	...
RbAr	5.82	3.60	...	...	3.60	8.57
Theo. (Ref. 32)	5.45	...	...	...	...	...
CsHe	6.93	3.44	4.87	9.21	3.44	10.58
Theo. (Ref. 30)	...	3.38	...	...	3.38	...
Theo. (Ref. 27)	...	3.49	...	...	3.49	...
CsNe	6.46	3.60	5.03	8.78	3.55	10.37
Theo. (Ref. 32)	6.46	...	...	...	...	...
CsAr	6.09	3.81	6.14	7.46	3.81	8.89
Exp. (Ref. 49)	5.50	...	...	...	...	...
Theo. (Ref. 31)	5.59	...	...	...	...	...
Theo. (Ref. 32)	5.59	...	...	...	...	...

well depths compared to the shallower ground state $X^2\Sigma^+_{1/2}$ well. Moreover, the minima of the two $A^2\Pi$ wells occur at approximately the same value of $R = r_{min} = r_{min1}$. In addition to exhibiting a minimum at $R = r_{min1}$ the $A^2\Pi_{1/2}$ curve also exhibits a local minimum of depth D_{min2} at $R = r_{min2}$ which is separated from the deep well by a barrier of height V_b at $R = r_b$.

The equilibrium positions of all wells and barriers for the PECs are tabulated in Table II and the well depths and barrier heights are tabulated in Table III. Where possible these are compared to experiment and other theoretical calculations. The equilibrium and barrier positions in Table II are all in agreement to within a few percent, and most values are in agreement to within 1%–2%. The well depths listed in Table III are in greatest disagreement with the DFT based calculations.[30,32] Excluding the DFT results, the well depths are in agreement to within about 20%–30% for the $X^2\Sigma^+_{1/2}$ curve and to within 5%–10% for the $A^2\Pi_{1/2}$ and $A^2\Pi_{3/2}$ curves. The larger relative error in the ground state well depths is primarily due to their smaller values.

The PECs for all M + Ng combinations are presented in Figures 3 through 6 and grouped by molecular term symbol. Figure 3 displays all $X^2\Sigma^+_{1/2}$ PECs, Figure 4 displays all $B^2\Sigma^+_{1/2}$ PECs, Figure 5 displays all $A^2\Pi_{1/2}$ PECs, and Figure 6 displays all $A^2\Pi_{3/2}$ PECs. In Figures 3 through 6, the PECs associated with one alkali are artificially offset from those of another for clarity. Potassium curves are asymptotically set to $0\,\mathrm{cm}^{-1}$, rubidium to $250\,\mathrm{cm}^{-1}$, and cesium to $500\,\mathrm{cm}^{-1}$.

The $X^2\Sigma^+_{1/2}$ ground curves shown in Figure 3 all exhibit shallow wells with minima in the range of $R \approx 5$–7 Å. The depths of these wells increase as the mass of the noble gas atom in the M + Ng pair increases. Also, for a given noble gas atom, the well depths are similar regardless of the alkali

atom with which it is paired. An exception to this trend occurs for K + Ar where the $X^2\Sigma^+_{1/2}$ well is deeper by a factor of one and a half when compared to the Rb + Ar and Cs + Ar $X^2\Sigma^+_{1/2}$ wells. The equilibrium position for these wells increases as the mass of the alkali atom increases. However for a given alkali atom, the equilibrium position of these wells decreases as the mass of the noble gas atom increases. This decrease in equilibrium position may be attributed to the increase in attractive dispersion force as the number of noble gas electrons increases.[50] A similar trend in the equilibrium position of the $X^2\Sigma^+_{1/2}$ ground curves was also observed by Goll et al..[32]

The excited $B^2\Sigma^+_{1/2}$ curves are shown in Figure 4. Each exhibits a shoulder at values of $R = 3$–5 Å and a very shallow well at values of $R = 7$–9 Å. These shallow $B^2\Sigma^+_{1/2}$ wells do not appear on the scale of the plot in Figure 4. An expanded view of this $B^2\Sigma^+_{1/2}$ well for Rb + Ar is shown in Figure 7, where the well appears at approximately the same value of R for which the $B^2\Sigma^+_{1/2}$ and $A^2\Pi_{3/2}$ curves diverge. The $B^2\Sigma^+_{1/2}$ shoulders occur highest up on the repulsive wall for potassium, followed by rubidium, and then cesium. For a given alkali atom, the shoulders are most pronounced for argon and lowest in energy, and least pronounced for helium and highest in energy. The neon shoulders are very similar to

TABLE III. Well depths and barrier heights (cm^{-1}), as defined in Figure 2, for all M + Ng curves. Note that a negative value for V_b corresponds to a local maximum that is less than the asymptotic $^2P_{1/2}$ atomic energy. The pseudopotential calculations by Pascale (Ref. 27) and the DFT calculations by Zbiri and Daul (Ref. 30) report energies for the $A^2\Pi$ curve and are listed under both the $A^2\Pi_{1/2}$ and $A^2\Pi_{3/2}$ columns for ease of comparison.

| M + Ng | $X^2\Sigma^+_{1/2}$ | $A^2\Pi_{1/2}$ | | | $A^2\Pi_{3/2}$ | $B^2\Sigma^+_{1/2}$ |
	D_e	D_{e1}	V_b	D_{e2}	D_e	D_e
KHe	−8.7	−199.3	1.6	−2.1	−220.6	−1.8
Theo. (Ref. 30)	...	−480	...	...	−480	...
Theo. (Ref. 27)	...	−245	...	...	−245	...
KNe	−17.1	−164.3	−1.9	−2.2	−184.8	−1.2
Theo. (Ref. 32)	−5.6	...	...	...	...	...
KAr	−60.2	−429.9	...	...	−450.8	−9.5
Exp. (Ref. 47)	−40.65	...	...	...	...	...
Exp. (Ref. 48)	−40.1(6)	−405(15)	...	...	−427(15)	−23
Theo. (Ref. 28)	−59	−421	...	...	−440	...
Theo. (Ref. 32)	−41.7	...	...	...	...	...
RbHe	−8.7	−95.9	20.0	−1.2	−159.1	−0.3
Theo. (Ref. 29)	...	−102.1	26.5	...	−176.8	...
Theo. (Ref. 30)	...	−276	...	...	−276	...
Theo. (Ref. 27)	...	−134	...	...	−134	...
RbNe	−14.4	−67.1	10.2	−1.2	−125.8	−0.7
Theo. (Ref. 32)	−5.0	...	...	...	...	...
RbAr	−49.0	−255.2	...	...	−315.7	−7.3
Theo (Ref. 32)	−38.6	...	...	...	...	...
CsHe	−9.6	6.3	57.7	−1.9	−125.5	−0.6
Theo. (Ref. 30)	...	−230	...	...	−230	...
Theo. (Ref. 27)	...	−112	...	...	−112	...
CsNe	−12.9	−14.1	34.7	−1.7	−128.4	−0.7
Theo. (Ref. 32)	−4.7	...	...	...	...	...
CsAr	−48.3	−192.8	−12.3	−16.6	−315.3	−8.1
Exp. (Ref. 49)	−45	...	...	...	...	...
Theo. (Ref. 31)	−39.6	...	...	...	...	...
Theo. (Ref. 32)	−39.6	...	...	...	...	...

FIG. 4. The $B^2\Sigma^+_{1/2}$ curves for all M + Ng pairs. Offsets are the same as in Figure 3.

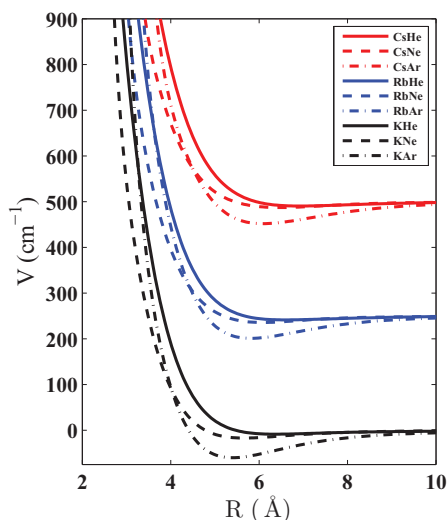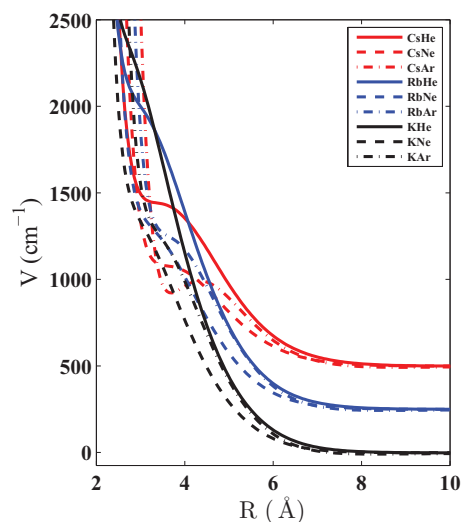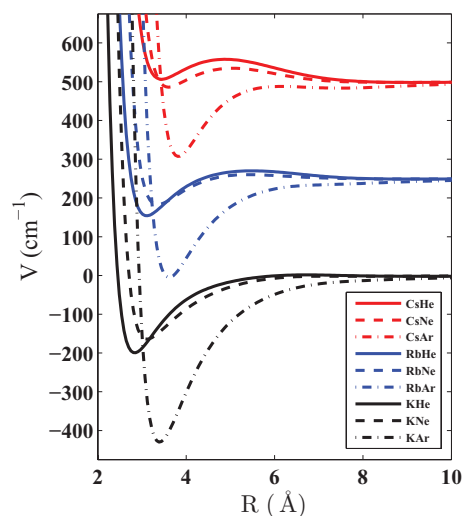FIG. 5. The $A^2\Pi_{1/2}$ curves for all M + Ng pairs. Offsets are the same as in Figure 3.

FIG. 3. The $X^2\Sigma^+_{1/2}$ curves for all M + Ng pairs. For clarity, the curves associated with one alkali atom are asymptotically offset from those of the other alkali atoms. The three K + Ng pairs are asymptotically set to zero, while the Rb + Ng are offset to 250 cm^{-1} and Cs + Ng are offset to 500 cm^{-1}.
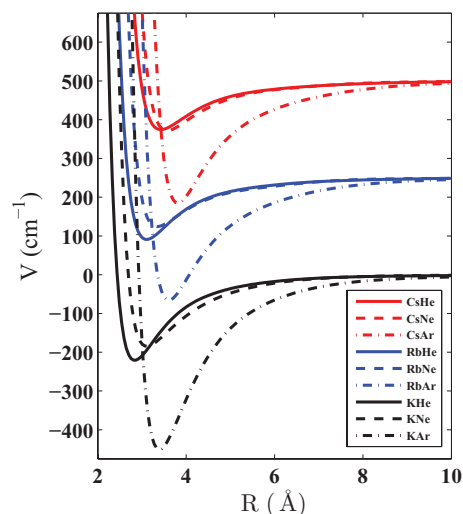

FIG. 6. The $A^2\Pi_{3/2}$ curves for all M + Ng pairs. Offsets are the same as in Figure 3.

argon and occur at roughly the same energies. For Cs + Ar this feature is so pronounced that the repulsive wall actually stops rising and decreases, forming a local minimum, before becoming repulsive again. These shoulders have been attributed by Pascale and Vandeplanque[51] to mixing with higher excited states that correlate in the dissociated atom limit to the $(n-1)^2D_{3/2}$ and $(n-1)^2D_{5/2}$ alkali manifolds.[52]

In Figure 5 each of the $A^2\Pi_{1/2}$ curves is qualitatively similar but demonstrates considerable quantitative variation. For a given alkali atom, the well depths D_{e1} are the deepest for Ar, shallowest for Ne, with He being somewhat deeper than Ne. An exception to this ordering is Cs where the He well is shallower than the Ne well. The equilibrium position $R = r_{min1}$ of the $A^2\Pi_{1/2}$ wells increases as either the alkali or noble gas mass increases. Since the $A^2\Pi_{1/2}$ minima lie closer to the repulsive wall than the $X^2\Sigma_{1/2}^+$ wells, Coulomb and exchange repulsion dominate, and polarization is less important. As a result the equilibrium positions increase with the atomic number of the noble gas atom rather than decrease as they do for the $X^2\Sigma_{1/2}^+$ curves. It is interesting to note that the $A^2\Pi_{1/2}$ well depths are linearly correlated to the difference of the average ionization energies of M and Ng from their first excited state manifolds. This suggests that there is a simple model for the $A^2\Pi$ well depth similar to charge-resonance models used to describe excimer luminescence.[53–55]

The barrier heights, V_b, of the $A^2\Pi_{1/2}$ curves can be used together with the well depths D_{e2} to compute a relative barrier height $V_b - D_{e2}$. This relative barrier height increases as the mass of the alkali atom increases. For a given alkali the relative barrier height also increases as the mass of the noble

gas atom decreases. These barriers at $R = r_b$ are accompanied by shallow wells at $R = r_{min2}$ and, together with the shallow wells exhibited by the $B^2\Sigma_{1/2}^+$ curves, are associated with radial derivative coupling between the $A^2\Pi_{1/2}$ and $B^2\Sigma_{1/2}^+$ states.[56] Note that a negative value for V_b corresponds to a local maximum that is less than the asymptotic $^2P_{1/2}$ atomic energy. Also, note that K + Ar and Rb + Ar are the only M + Ng combinations whose $A^2\Pi_{1/2}$ curves do not exhibit a barrier.

The $A^2\Pi_{3/2}$ curves shown in Figure 6 are similar to the $A^2\Pi_{1/2}$ curves. The $A^2\Pi_{3/2}$ well depths, D_e, follow the same trend as the $A^2\Pi_{1/2}$ well depths, D_{e1}, with regard to the mass of the alkali and noble gas atoms. The $A^2\Pi_{3/2}$ curves differ from the $A^2\Pi_{1/2}$ curves in that D_e is greater than D_{e1} for all nine M + Ng pairs, and the $A^2\Pi_{3/2}$ curves exhibit no secondary minima. The absence of secondary minima occurs because there is no radial derivative coupling between the $A^2\Pi_{3/2}$ states and other states nearby in energy. It is interesting to note that the equilibrium positions of the wells in both the $A^2\Pi_{1/2}$ and $A^2\Pi_{3/2}$ curves are nearly equal to each other and to the minimum of the $A^2\Pi$ curve obtained when spin-orbit coupling is neglected.

An analysis of the vibrational energy levels (VELs) for the M + Ng systems show that all $X^2\Sigma_{1/2}^+$, $A^2\Pi_{1/2}$, and $A^2\Pi_{3/2}$ curves exhibit weakly bound vibrational states. The VELs are computed with a finite basis representation of the vibrational Hamiltonian, where the rotational degree of freedom is ignored ($J = 0$). Vibrational spectra have been observed for the $A^2\Pi_{3/2}$ electronic state of Rb + He,[57] the ground $X^2\Sigma_{1/2}^+$ and excited $A^2\Pi$ electronic states for K + Ar,[48] and the $A^2\Pi_{1/2}$ and $A^2\Pi_{3/2}$ curves of Cs + He.[58] Hirano et al.[29] have computed VELs for the $A^2\Pi_{3/2}$ curve of

TABLE IV. Rb + He $A^2\Pi_{3/2}$ vibrational energy level differences (in cm^{-1}) for $\Delta v = 1$.

ΔE	This Work	Exp. (Ref. 57)	Hirano (Ref. 29)
$E_1 - E_0$	55.47	65.8(3)	60.5
$E_2 - E_1$	33.10	43.7(2)	39.2
$E_3 - E_2$	17.72	23.2(7)	18.2
$E_4 - E_3$	9.57	8.8(6)	11.9
$E_5 - E_4$	4.47	…	7.9

TABLE V. K + Ar $X^2\Sigma^+$ and $A^2\Pi$ vibrational energy level differences in cm^{-1} for $\Delta v = 1$.

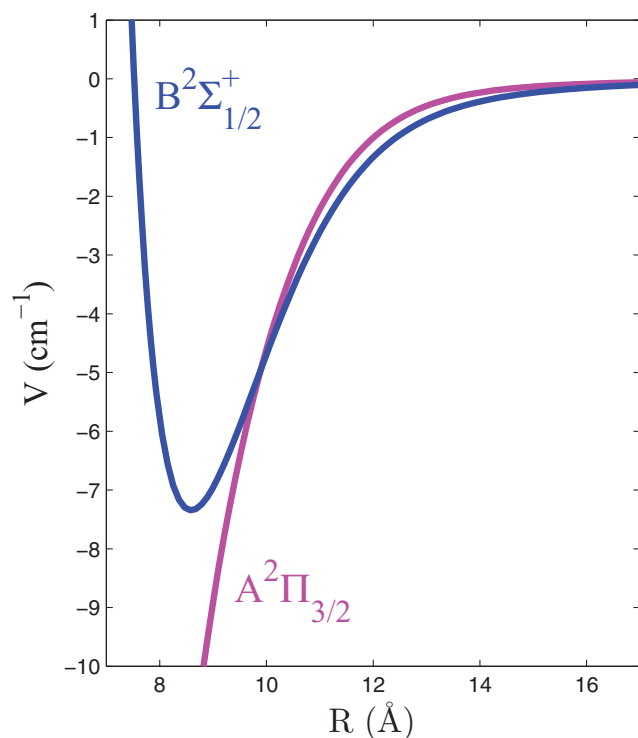| ΔE	This Work $X^2\Sigma_{1/2}^+$	Exp. (Ref. 48) $X^2\Sigma$	This Work $A^2\Pi_{3/2}$	This Work $A^2\Pi_{1/2}$	Exp. (Ref. 48) $A^2\Pi$
$E_1 - E_0$	9.55	8.77			
$E_2 - E_1$	8.69	7.53			
$E_3 - E_2$	7.77	6.25			
$E_7 - E_6$			27.24	27.41	26.45
$E_8 - E_7$			24.07	24.27	22.86
$E_9 - E_8$			21.11	21.35	19.57
$E_{10} - E_9$			18.38	18.69	16.55
$E_{11} - E_{10}$			15.91	16.31	13.63

FIG. 7. An expanded view of the $B^2\Sigma_{1/2}^+$ well for Rb + Ar. The well occurs where the $B^2\Sigma_{1/2}^+$ and $A^2\Pi_{3/2}$ PECs diverge. Similar behavior is observed for all M + Ng pairs.

TABLE VI. Cs + He $A^2\Pi_{1/2}$ and $A^2\Pi_{3/2}$ vibrational energy levels in cm^{-1} relative to the Cs $^2P_{1/2}$ and $^2P_{3/2}$ levels, respectively. The $A^2\Pi_{1/2}$ curve exhibits a single quasibound state with a positive VEL.

Electronic state	Vibrational state	This Work	Exp. (Ref. 58)
$A^2\Pi_{1/2}$	$\nu = 0$	50.0	48.35
$A^2\Pi_{3/2}$	$\nu = 0$	-95.0	-84.89
	$\nu = 1$	-51.1	-45.09
	$\nu = 2$	-25.1	-19.79
	$\nu = 3$	-11.6	-5.90
	$\nu = 4$	-4.0	-0.51
	$\nu = 5$	-0.3	$\ldots$

Rb + He. The difference between VELs for $\Delta\nu = 1$ are tabulated in Table IV for Rb + He and Table V for K + Ar, while the absolute VELs measured from dissociation are tabulated in Table VI for Cs + He.

As listed in Table IV, the computational results predict the presence of six VELs for the Rb + He $A^2\Pi_{3/2}$ curve, however, only five levels are observed. The experimental differences listed in this table were fit by Mudrich *et al.*[57] to a Morse potential. The Morse fit is compared with the $A^2\Pi_{3/2}$ curve in Figure 8. The Morse potential exhibits a deeper well, while our $A^2\Pi_{3/2}$ curve approaches equilibrium more slowly. The VELs are included in Figure 8 for comparison purposes.

Our calculations of the K + Ar $X^2\Sigma_{1/2}^+$ VELs indicate that there are 12 bound vibrational states. The first three VEL differences for $\Delta\nu = 1$ are listed in Table V. These calculations also indicate that the K + Ar $A^2\Pi_{1/2}$ curve has 22 bound
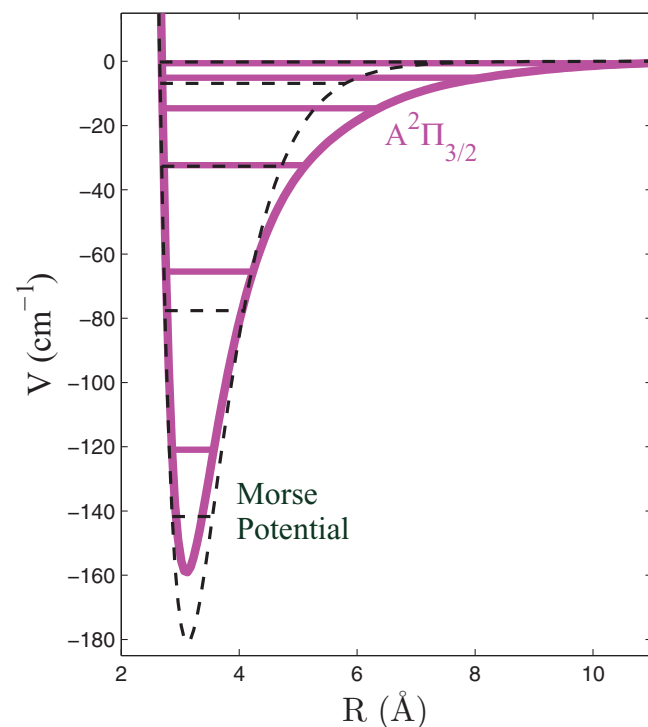

FIG. 8. The Rb + He $A^2\Pi_{3/2}$ curve (solid) and a Morse potential fit (dashed) to the experimental vibrational energy differences listed in Table IV (Ref. 57). The curves are offset to share a common asymptotic limit, and vibrational energy levels are included for comparison.

vibrational states, and the $A^2\Pi_{3/2}$ curve has 24. Several $\Delta\nu = 1$ VEL differences for the $A^2\Pi_{1/2}$ and $A^2\Pi_{3/2}$ curves are also listed in Table V where ν ranges from six to ten. Theoretical $\Delta\nu = 1$ values are listed in Table V only if there is a corresponding experimental value for comparison. The VELs predicted for the $A^2\Pi_{1/2}$ and $A^2\Pi_{3/2}$ curves are nearly the same, being most similar for the lower VELs. This reflects the similarity between the $A^2\Pi_{1/2}$ and $A^2\Pi_{3/2}$ curves that occurs because the $A^2\Pi_{1/2}$ curve for K + Ar has only one local minimum for all R. The experimental results tabulate $\Delta\nu = 1$ VEL differences for the $A^2\Pi$ level.

Experimental and calculated VELs are listed in Table VI for the $A^2\Pi_{1/2}$ and $A^2\Pi_{3/2}$ curves of Cs + He. As seen in Figure 5, the bottom of the Cs + He $A^2\Pi_{1/2}$ well lies above its asymptotic energy. However, calculations predict that this well does support one quasibound VEL which has also been experimentally observed.[58] The $A^2\Pi_{3/2}$ curve is predicted to support six bound VELs as compared to five experimentally observed VELs. Note that predictions for the VELs of $A^2\Pi_{1/2}$ and $A^2\Pi_{3/2}$ curves of K + Ar are very similar, while predictions for the same two curves of Cs + He are significantly different. This reflects the trend for the relative barrier height $V_b - D_{e2}$ to increase as the mass of the alkali atom increases and the mass of the noble gas decreases. As the relative barrier height increases, the $A^2\Pi_{1/2}$ and $A^2\Pi_{3/2}$ curves become more dissimilar causing a greater disparity between the corresponding VELs.

The PECs of M + Ng pairs can be used to predict alkali line shapes that are broadened by collisions with noble gas atoms.[25,26] In the semi-classical Anderson-Talman model of line broadening, the alkali D1 and D2 line shapes are governed in part by difference potentials, ΔV, given by the difference between PECs. In case of the D1 line, the $A^2\Pi_{1/2}$ curve correlates with the $^2P_{1/2}$ atomic energy level, and the line shape is determined by the single difference potential, $\Delta V = A^2\Pi_{1/2} - X^2\Sigma_{1/2}^+$, when non-adiabatic effects are ignored. For the D2 line, both the $A^2\Pi_{3/2}$ and the $B^2\Sigma_{1/2}^+$ curves correlate with the $^2P_{3/2}$ atomic energy level, and the line shape is therefore determined by two difference potentials, $\Delta V = A^2\Pi_{3/2} - X^2\Sigma_{1/2}^+$ and $\Delta V = B^2\Sigma_{1/2}^+ - X^2\Sigma_{1/2}^+$. When non-adiabatic effects are included, all four PECs are expected to contribute to both the D1 and D2 line broadening.

To better understand the general shape of the difference potentials, four plots for Cs + Ar are shown in Figure 9 using a common R axis. The first plot at the top of the figure shows the excited $A^2\Pi_{1/2}$, $A^2\Pi_{3/2}$, and $B^2\Sigma_{1/2}^+$ curves, while the second plot from the top of the figure shows the ground $X^2\Sigma_{1/2}^+$ curve. The PECs in the first plot use the same zero as the second plot and, as mentioned before, are offset in the asymptotic limit $R = 100$ Å to the alkali D1 and D2 NIST values.[41] The third plot from the top shows the $\Delta V = A^2\Pi_{1/2} - X^2\Sigma_{1/2}^+$, $\Delta V = A^2\Pi_{3/2} - X^2\Sigma_{1/2}^+$, and $\Delta V = B^2\Sigma_{1/2}^+ - X^2\Sigma_{1/2}^+$ difference potentials in units of nm. Finally, the transition dipole moments $|\langle X^2\Sigma_{1/2}^+|D|A^2\Pi_{1/2}\rangle|$, $\langle X^2\Sigma_{1/2}^+|D|A^2\Pi_{3/2}\rangle|$, and $|\langle X^2\Sigma_{1/2}^+|D|B^2\Sigma_{1/2}^+\rangle|$ are shown in the fourth plot at the bottom of the figure. Similar to the PECs, the dipole matrix elements are offset using the NIST Einstein A coefficients.[41]
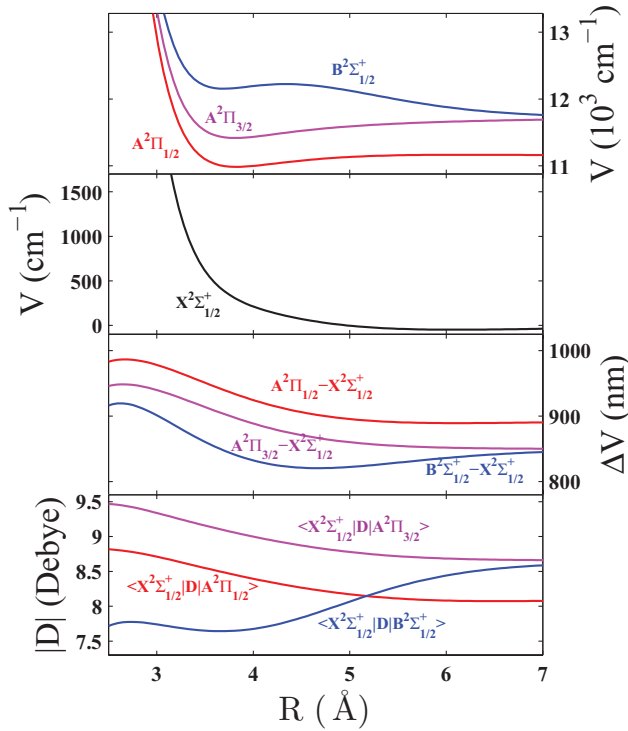
FIG. 9. The Cs + Ar $B^2\Sigma_{1/2}^+$, $A^2\Pi_{1/2}$, and $A^2\Pi_{3/2}$ curves are shown in the first plot, and the second plot shows the $X^2\Sigma_{1/2}^+$ curve. The potential energy curves use the same zero as the second plot and are offset in the asymptotic limit to the alkali D1 and D2 values (Ref. 41). The third plot shows potential differences and the fourth plot shows transition dipole matrix elements.

Difference potentials ΔV can be used to compute collisionally broadened line shapes, $I(\omega)$, in the quasistatic limit[25,26,59] where

$$I(\omega) \propto \sum_c R_c^2 |D(R_c)|^2 \left| \frac{d(\Delta V)}{dR} \right|_{R_c}^{-1}$$
$$\times n_{Ng} \exp\left(-\frac{X^2\Sigma_{1/2}^+(R_c)}{k_B T} \right). \quad (1)$$

In Eq. (1), $D(R_c)$ is the transition dipole matrix element, n_{Ng} is the concentration of the noble gas, k_B is Boltzmann's constant, T is the absolute temperature, $X^2\Sigma_{1/2}^+(R_c)$ is the ground state PEC, and $R_c(\omega)$ are Condon points given by the solutions to the equation $\Delta V(R_c) = \hbar\omega$.[25] Here it is assumed that the concentration of the alkali gas is low relative to n_{Ng}, and the line broadening occurs only as a result of M + Ng collisions.

For a given value of ω, the Boltzmann factor in Eq. (1) governs the probability for which a given M + Ng pair will be at a separation distance $R_c(\omega)$. The product of the Boltzmann factor and n_{Ng} defines an effective concentration, $n_{eff}(R_c)$, and for Cs + Ar at $T = 400$ K this corresponds to $n_{eff}(3.5\,\text{Å}) \approx 0.1 n_0$. Because the Boltzmann factor drops off rapidly at lower values of R_c, this term dominates the expression for $I(\omega)$ for values of $R_c < 3.5$. For a given value of ω for which $R_c(\omega) > 3.5$ the intensity will depend on the value of the dipole matrix element and the derivative of the difference potential. In Figure 9, the Cs + Ar dipole matrix elements vary on the order of 5%–10% for R ranging from $R = 3.5$ to the asymptotic limit. The difference potentials for

Cs + Ar in Figure 9 exhibit extrema that correspond to singularities in $I(\omega)$ as given by Eq. (1). The $B^2\Sigma_{1/2}^+ - X^2\Sigma_{1/2}^+$ difference potential exhibits three extrema, one in the asymptotic limit, one at $R \approx 4.5$, and one at $R \approx 2.6$. The extremum in the asymptotic limit corresponds to the D2 atomic line core, and the extremum at $R \approx 4.5$ corresponds to a satellite blue shifted from line core. The extremum at $R \approx 2.6$ corresponds to a red shifted satellite, however, it is allowed by the Boltzmann distribution only at sufficiently high temperatures. The $A^2\Pi_{1/2} - X^2\Sigma_{1/2}^+$ and $A^2\Pi_{3/2} - X^2\Sigma_{1/2}^+$ difference potentials also exhibit extrema in the asymptotic limit corresponding to the D1 and D2 line cores, respectively, and extrema at small values of R corresponding to red shifted satellites that are suppressed by the Boltzmann distribution.

Predictions for the positions of blue shifted satellites of the D2 alkali transitions are reported in Table VII along with comparisons to experiment. The predicted satellite peaks are all shifted in the blue direction from the observed satellite peaks by approximately 12−20 nm. The predicted satellite peaks occur as a result of the shoulder exhibited by the $B^2\Sigma_{1/2}^+$ curves. For the Stuttgart basis set used in these calculations, it is likely that this shoulder is not accurately computed, which gives rise to the discrepancy between predicted and observed blue satellites. However, our calculations do capture the trends observed in the experimental data. As seen in Table VII, the experimentally observed satellite peak for Cs + He at 827 nm is significantly more blue shifted than the peaks for Cs + Ne and Cs + Ar at 837 and 838 nm, respectively. Our theoretical predictions mirror this pattern where, for a given alkali atom, the blue peaks for neon and argon are relatively close in wavelength and the helium peak is significantly more blue shifted. These peaks correspond to the $B^2\Sigma_{1/2}^+$ shoulder that, as seen in Figure 4, occurs highest in energy for M + He and at lower but similar energies for M + Ne and M + Ar. For rubidium the experimental data identifies neon and argon satellites at 752 and 754 nm, respectively, while no experimental data could be found for helium. It is possible to make a prediction for the Rb + He satellite by computing the difference between the calculated Rb + Ne and Rb + He satellites in Table VII and subtracting it from the experimental Rb + Ne satellite. This procedure yields 733 nm for the Rb + He satellite peak. The same procedure applied to cesium yields 825 nm for the Cs + He satellite compared to the experimental value of 827 nm. For potassium no experimental data could be found. However, the surfaces suggest that the K + He satellite will be significantly more blue shifted than the K + Ne and K + Ar satellites. A second trend in Table VII is observed where, for a given noble gas atom, the satellite is more blue shifted as the mass of the alkali atom decreases. This corresponds to $B^2\Sigma_{1/2}^+$ shoulders in Figure 4 which occur highest in energy for K + Ng, followed by Rb + Ng, and lowest in energy for Cs + Ng.

CONCLUSIONS

In this paper we calculate ground and excited state potential energy curves for nine different M + Ng pairs. The curves are obtained via a state-averaged multi-configurational self-consistent field calculation followed by a spin-orbit

TABLE VII. Positions (nm) of blue shifted satellites associated with the difference potentials $B^2\Sigma_{1/2}^+ - X^2\Sigma_{1/2}^+$ extrema. The D2 column lists the atomic alkali transition.

M+Ng	D2 (Ref. 41)	This Work	Exp. (Ref. 60)	Exp. (Ref. 61)	Exp. (Ref. 11)	Exp. (Ref. 62)
KHe		692.7				
KNe	764.7	718.0				
KAr		713.7				
RbHe		720.5				
RbNe	778.2	739.9	754	752		
RbAr		736.2	755.5	754		
CsHe		810.9				827
CsNe	850.1	822.8			837	837
CsAr		820.6				838

multi-reference singles and doubles configuration interaction calculation. Davidson-Silver corrections are made to the potential energy curves and transition dipole moments are computed.

The same level of theory is used for all calculations and facilitates the identification of trends that occur as different alkali atoms and noble gas atoms are considered. These trends are confirmed through a variety of experimental observations including spectroscopic parameters, vibrational energy levels, and collisionally broadened D1 and D2 lines. In particular we are able to predict trends in the position of the collisionally induced D2 satellite peak and, using our calculations together with experimental data, make a prediction for the absolute position of the Rb + He satellite peak.

The largest source of error in these calculations is likely to be basis set incompleteness error, and improvements to the potential energy curves can be made through the consideration of a hierarchy of basis sets, both with and without counterpoise corrections, to explore the complete basis set limit.

Both ground and excited state potential energy curves for alkali atom and noble gas atom pairs are useful for predicting a wide variety of behaviors including non-adiabatic coupling,[63,64] cross sections for fine structure transitions,[64] and collisionally induced spectral broadening.[25,26] Potential energy curves and dipole matrix elements are included as supplementary material with this paper.[65]

ACKNOWLEDGMENTS

[1]W. Krupke, R. Beach, V. Kanz, and S. Payne, Opt. Lett. **28**, 2336 (2003).

[2]R. J. Beach, W. F. Krupke, V. K. Kanz, and S. A. Payne, J. Opt. Soc. Am. B **21**, 2151 (2004).

[3]B. V. Zhdanov, T. Ehrenreich, and R. J. Knize, Opt. Commun. **260**, 696 (2006).

[4]R. H. Page, R. J. Beach, V. K. Kanz, and W. F. Krupke, Opt. Lett. **31**, 353 (2006).

[5]B. V. Zhdanov, J. Sell, and R. J. Knize, Electron. Lett. **44**, 582 (2008).

[6]M. Rotondaro and G. Perram, J. Quant. Spectrosc. Radiat. Transf. **57**, 497 (1997).

[7]G. Pitz, D. Wertepny, and G. Perram, Phys. Rev. A **80**, 062718 (2009).

[8]G. Pitz, C. Fox, and G. Perram, Phys. Rev. A **82**, 042502 (2010).

[9]J. D. Readle, C. J. Wagner, J. T. Verdeyen, D. L. Carroll, and J. G. Eden, Electron. Lett. **44**, 1466 (2008).

[10]J. D. Readle, J. T. Verdeyen, J. G. Eden, S. J. Davis, K. L. Galbally-Kinney, W. T. Rawlins, and W. J. Kessler, Opt. Lett. **34**, 3638 (2009).

[11]J. D. Readle, C. J. Wagner, J. T. Verdeyen, T. M. Spinka, D. L. Carroll, and J. G. Eden, Appl. Phys. Lett. **94**, 251112 (2009).

[12]A. D. Palla, D. L. Carroll, J. T. Verdeyen, J. D. Readle, T. M. Spinka, C. J. Wagner, J. G. Eden, and M. C. Heaven, Proc. SPIE **7581**, 75810L (2010).

[13]J. Readle, C. Wagner, J. Verdeyen, T. Spinka, D. Carroll, and J. Eden, Proc. SPIE **7581**, 75810K (2010).

[14]A. D. Palla, D. L. Carroll, J. T. Verdeyen, and M. C. Heaven, Proc. SPIE **7915**, 79150B (2011).

[15]A. D. Palla, D. L. Carroll, J. T. Verdeyen, and M. C. Heaven, J. Phys. B **44**, 135402 (2011).

[16]S. Seager and D. D. Sasselov, Astrophys. J. **537**, 916 (2000).

[17]A. Burrows, W. B. Hubbard, J. I. Lunine, and J. Liebert, Rev. Mod. Phys. **73**, 719 (2001).

[18]T. M. Brown, Astrophys. J. **553**, 1006 (2001).

[19]A. Burrows, A. J. Burgasser, J. D. Kirkpatrick, J. Liebert, J. A. Milsom, D. Sudarsky, and I. Hubeny, Astrophys. J. **573**, 394 (2002).

[20]A. J. Burgasser, J. D. Kirkpatrick, J. Liebert, and A. Burrows, Astrophys. J. **594**, 510 (2003).

[21]C. Zhu, J. F. Babb, and A. Dalgarno, Phys. Rev. A **71**, 052710 (2005).

[22]C. Zhu, J. F. Babb, and A. Dalgarno, Phys. Rev. A **73**, 012506 (2006).

[23]N. F. Allard, J. F. Kielkopf, and F. Allard, Eur. Phys. J. D **44**, 507 (2007).

[24]R. Santra and K. Kirby, J. Chem. Phys. **123**, 214309 (2005).

[25]J. Szudy and W. Baylis, Phys. Rep. **266**, 127 (1996).

[26]N. Allard and J. Kielkopf, Rev. Mod. Phys. **54**, 1103 (1982).

[27]J. Pascale, Phys. Rev. A **28**, 632 (1983).

[28]M. B. E. H. Rhouma, H. Berriche, Z. B. Lakhdar, and F. Spiegelman, J. Chem. Phys. **116**, 1839 (2002).

[29]K. Hirano, K. Enomoto, M. Kumakura, Y. Takahashi, and T. Yabuzaki, Phys. Rev. A **68**, 012722 (2003).

[30]M. Zbiri and C. Daul, J. Chem. Phys. **121**, 11625 (2004).

[31]J. M. Merritt, J. Han, T. Chang, and M. C. Heaven, Proc. SPIE **7196**, 71960H (2009).

[32]E. Goll, H. Werner, H. Stoll, T. Leininger, P. Gori-Giorgi, and A. Savin, Chem. Phys. **329**, 276 (2006).

[33]H. Lischka, R. Shepard, F. B. Brown, and I. Shavitt, Int. J. Quantum Chem., Quantum Chem. Symp. **S15**, 91 (1981).

[34]R. Shepard, I. Shavitt, R. M. Pitzer, D. C. Comeau, M. Pepper, H. Lischka, P. G. Szalay, R. Ahlrichs, F. B. Brown, and J. Zhao, Int. J. Quantum Chem., Quantum Chem. Symp. **22**, 149 (1988).

[35]H. Lischka, R. Shepard, R. M. Pitzer, I. Shavitt, M. Dallow, Th. Müller, P. G. Szalay, M. Seth, G. S. Kedziora, S. Yabushita, and Z. Zhang, Phys. Chem. Chem. Phys. **3**, 664 (2001).

[36]H. Lischka, R. Shepard, I. Shavitt, R. M. Pitzer, M. Dallos, Th. Müller, P. G. Szalay, F. B. Brown, R. Ahlrichs, H. J. Böhm, A. Chang, D. C. Comeau, R. Gdanitz, H. Dachsel, C. Ehrhardt, M. Ernzerhof, P. Höchtl, S. Irle, G. Kedziora, T. Kovar, V. Parasuk, M. J. M. Pepper, P. Scharf, H. Schiffer, M. Schindler, M. Schüler, M. Seth, E. A. Stahlberg, J. G. Zhao, S. Yabushita, Z. Zhang, M. Barbatti, S. Matsika, M. Schuurmann, D. R. Yarkony, S. R. Brozell, E. V. Beck, and J. P. Blaudeau, COLUMBUS, an *ab initio* electronic structure program, Release 5.9.1 (2006).

[37]S. Yabushita, Z. Zhang, and R. M. Pitzer, J. Phys. Chem. A **103**, 5791 (1999).

[38]I. S. Lim, P. Schwerdtfeger, B. Metz, and H. Stoll, J. Chem. Phys. **122**, 104103 (2005).

[39]F. Weigend and R. Ahlrichs, Phys. Chem. Chem. Phys. **7**, 3297 (2005).

[40]L. Blank, G. S. Kedziora, and D. E. Weeks, Proc. SPIE **7581**, 75810I1 (2010).

[41]Y. Ralchenko, A. E. Kramida, J. Reader, and NIST ASD Team, NIST Atomic Spectral Database, version 4.1.0, National Institute of Standards and Technology, Gaithersburg, MD, 2011, see http://physics.nist.gov/asd3.

[42]E. R. Davidson and D. W. Silver, Chem. Phys. Lett. **52**, 403 (1977).

[43]S. F. Boys and F. Bernardi, Mol. Phys. **19**, 553 (1970).

[44]S. Iwata, J. Chem. Phys. **135**, 094101 (2011).

[45]T. Helgaker, P. Jorgensen, and J. Olsen, *Molecular Electronic-Structure Theory* (Wiley, 2000).

[46]R. M. Balabin, J. Chem. Phys. **132**, 211103 (2010).

[47]C. Figl, J. Grosser, O. Hoffmann, and F. Rebentrost, J. Phys. B **37**, 3369 (2004).

[48]F. Bokelmann and D. Zimmermann, J. Chem. Phys. **104**, 923 (1996).

[49]U. Buck and H. Pauly, Zeit. F. Phys. **208**, 390 (1968).

[50]A. J. Stone, *The Theory of Intermolecular Forces* (Clarendon Press, Oxford, 1996).

[51]J. Pascale and J. Vandeplanque, J. Chem. Phys. **60**, 2278 (1974).

[52]M. Ehara and H. Nakatsuji, J. Chem. Phys. **102**, 6822 (1995).

[53]S. Shirai, S. Iwata, T. Tani, and S. Inagaki, J. Phys. Chem. A **115**, 7687 (2011).

[54]M. Nowakowska, M. Smoluch, and P. Petelenz, Chem. Phys. Lett. **270**, 234 (1997).

[55]Y. L. Chow and C. I. Johansson, J. Phys. Chem. **99**, 17558 (1995).

[56]F. H. Mies, Phys. Rev. A **7**, 942 (1973).

[57]M. Mudrich, F. Stienkemeier, G. Droppelmann, P. Claas, and C. P. Schulz, Phys. Rev. Lett. **100**, 023401 (2008).

[58]K. Enomoto, K. Hirano, M. Kumakura, Y. Takahashi, and T. Yabuzaki, Phys. Rev. A **66**, 042505 (2002).

[59]J. Szudy and W. Baylis, J. Quant. Spectrosc. Radiat. Transf. **15**, 641 (1975).

[60]C. G. Carrington and A. Gallagher, Phys. Rev. A **10**, 1464 (1974).

[61]D. L. Drummond and A. Gallagher, J. Chem. Phys. **60**, 3426 (1974).

[62]R. E. M. Hedges, D. L. Drummond, and A. Gallagher, Phys. Rev. A **6**, 1519 (1972).

[63]L. T. Belcher, "Gradients and non-adiabatic derivative coupling terms for spin-orbit wavefunctions," Ph.D. dissertation (Air Force Institute of Technology, 2011).

[64]C. D. Lewis, "Non-adiabatic atomic transitions: Computational cross section calculations of alkali metal-nobel gas collisions," Ph.D. dissertation (Air Force Institute of Technology, 2011).

[65]See supplementary material at http://dx.doi.org/10.1063/1.3696377 for potential energy curves and dipole matrix elements for all nine M + Ng pairs.